Chapter 2

SYNTHESIS AND CHARACTERIZATIONS

2.1 Introduction

This chapter presents the methodology of synthesis techniques, detailing of Rietveld refinement technique for analysing crystal structures, studies of electronic structures through density functional theory (DFT) and magnetic characterizations. $Ho_2Ge_xTi_{2-x}O_7$ towards the titanium side, (Pyrotitanates) crystallizes in cubic phase with $Fd\bar{3}m$ space group under ambient preparation condition, having typical pyrochlore structure [27]; whereas towards the germanium side, (Pyrogermanates) it belongs to tetragonal lattice class with $P4_12_12$ space group under ambient preparation condition [62], [67], [68]. Stability-field map illustrates the preparation condition depending upon the ionic radii of A (rare-earth ion) and B (transition metal ion) site element as discussed in Section 2.2. In Section 2.3 we will be discussing the synthesis of parent as well as the chemical pressure derivatives of $Ho_2Ge_2O_7$ and $Ho_2Ti_2O_7$. Section 2.4 will be dealing with the characterization techniques used in the present work for studying the system properties.

In $Ho_2Ge_2O_7$ negative chemical pressure can be applied by fractional substitution of Ti^{4+} having higher ionic radii at Ge^{4+} site. In the similar manner positive chemical pressure is applied in $Ho_2Ti_2O_7$ through the substitution of Ge^{4+} with smaller ionic radii than Ti^{4+} resulting in a series $Ho_2Ge_xTi_{2-x}O_7$ as shown in **Figure 2.1** [28], [58].

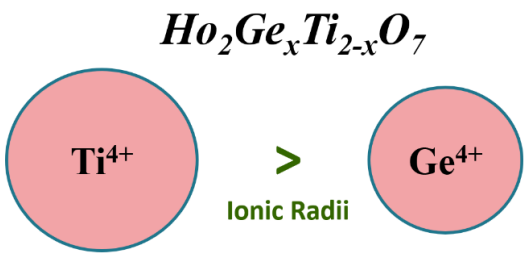

Figure 2.1 In the sample series $Ho_2Ge_xTi_{2-x}O_7$, positive and negative chemical pressure has been applied through the substitution of Ge^{4+} in $Ho_2Ti_2O_7$ and Ti^{4+} in $Ho_2Ge_2O_7$ respectively.

2.2 Stability-field/Structure-stability Map for the synthesis of $A_2B_2O_7$ materials

Geometric frustration plays a crucial role in the underlying physics of spin relaxation phenomena. In the search for new materials, the R_A/R_B cation radius ratio determines the stability of the pyrochlore lattice over the defect fluorite structure in the lower limit. Under ambient pressure, the pyrochlores are stable for $1.36 \leq R_A/R_B \leq 1.71$. **Figure 2.2** shows the possibility of the all the elements that could produce $A_2^{3+}B_2^{4+}O_7^{2-}$cubic pyrochlore phase. **Figure 2.3** displays the stability regime map of pyrochlores in the space of ionic radii [18]. It can be noticed that pyrochlore phase is not stable for all A for a given B, rather the stability is decided by the ionic radius ratio $R_A{}^{3+}/ R_B{}^{4+}$. The only transition element to form stable pyrochlore with all the rare-earth ion is B = Sn. For the smallest ionic radii at B site, only Mn^{4+} forms the pyrochlore phase under high-pressure synthesis conditions. The first stable series of pyrochlore is formed for B = V with only three rare-earth ions (A = Lu, Yb & Tm). The combination of element having largest ionic radii at B site and smallest at A site resulting into a stable pyrochlore is $Gd_2Pb_2O_7$.

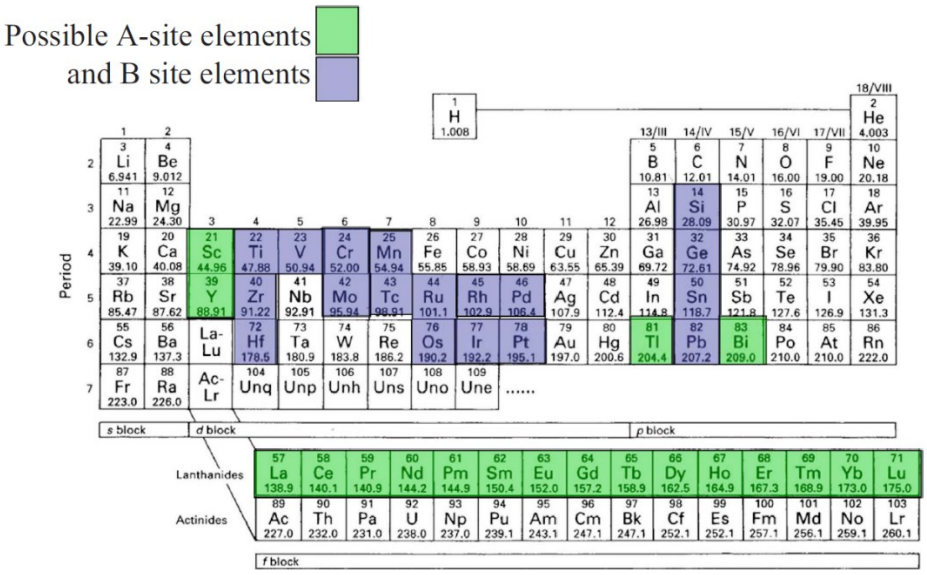

Figure 2.2 Possibility of the all the elements that could produce $A_2^{3+}B_2^{4+}O_7^{2-}$ cubic pyrochlore phase. [18]

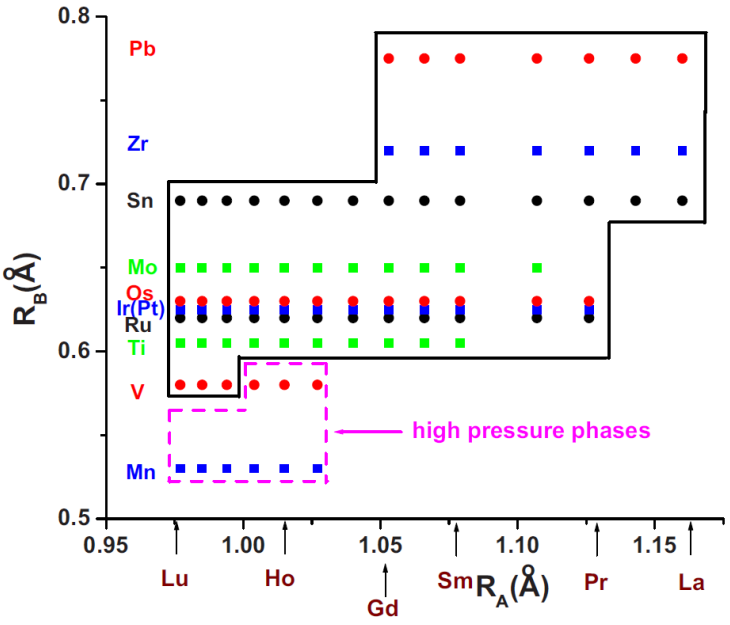

Figure 2.3 Stability field map for the synthesis of $A_2B_2O_7$ magnetically frustrated systems. [18]

We have synthesized a rare-earth pyrotitanate ($Ho_2Ti_2O_7$) and rare-earth pyrogermanate ($Ho_2Ge_2O_7$) system. The former is a stable pyrochlore, while the latter lies outside the stability regime since R_A/R_B for $Ho_2Ge_2O_7$ is 1.81. The inclusion of Ge^{4+} at Ti^{4+} site in $Ho_2Ti_2O_7$ can shift this crystallographically ordered system outside the stability regime which could affect the elementary spin dynamics. Subsequently, $Ho_2Ge_xTi_{2-x}O_7$ series has been synthesized with varying x through standard solid-state preparation method.

2.3 Solid–state synthesis route

Figure 2.4 shows the flowchart for the stepwise procedure adopted for sample synthesis.

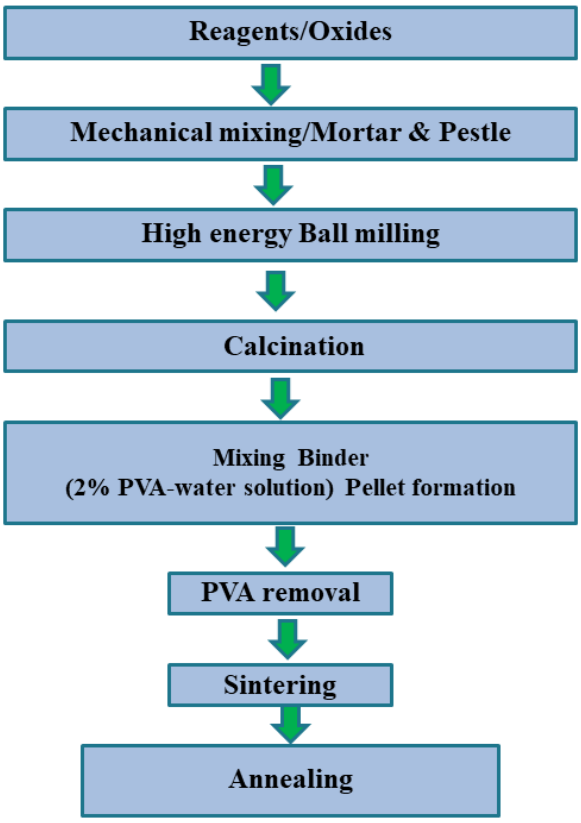

Figure 2.4 Flowchart for standard solid-state route adopted for the sample synthesis.

Polycrystalline sample of $Ho_2Ge_xTi_{2-x}O_7$ (x = 0, 0.05, 0.1, 0.15, 0.25, 0.5, 1, 1.5, 1.75, 1.9 & 2) series has been synthesized through standard solid-state route in which reagents were homogenously mixed followed by heat treatment to facilitate thermo-chemical reactions between them. Ho_2O_3 (> 99.9% assay, Sigma Aldrich), GeO_2 (> 99.999% assay, Sigma Aldrich) and TiO_2(> 99.8% assay, Sigma Aldrich) were taken in stoichiometric ratio and set for mechanical mixing for homogenization (10 hours) in high energy ball-mill using ethanol as mixing medium. The resulting slurry has been dried at room temperature. The obtained powder was calcined for 24 hours at 1300° C in alumina crucible to facilitate thermo-chemical reaction. It was regrounded into fine powder using an agate mortar-pestle, followed by mixing with polyvinyl alcohol (PVA), which acts as binding agent for the formation of pellet. Pellets underwent heat treatment at 600° C for 12 hours for binder removal. Further, these were sintered at 1350° C for 24 hours for densification. Finally, these pellets were crushed to fine powder and further annealed at 600 °C for 12 hours to remove the introduced strain during crushing. Homogenous composition of powdered samples has been used for further characterizations. **Figure 2.5** shows the obtained room temperature HRXRD pattern for $Ho_2Ge_xTi_{2-x}O_7$ for x = 2, 1.9, 1.75, 1.5 &1and **Figure 2.6** for that of x = 0, 0.05, 0.1, 0.15, 0.25 & 0.5.

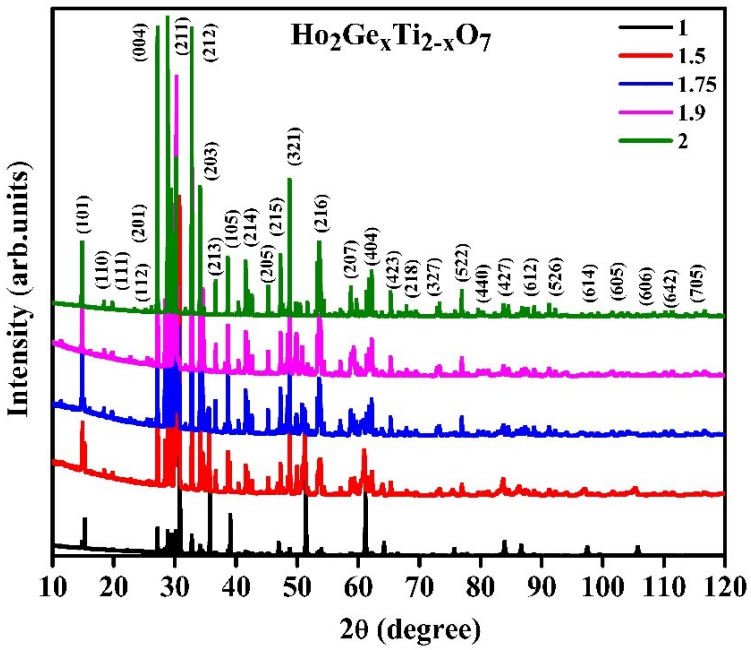

Figure 2.5 Room temperature high resolution x-ray diffraction pattern HRXRD pattern for $Ho_2Ge_xTi_{2-x}O_7$ (x = 2, 1.9, 1.75, 1.5 &1).

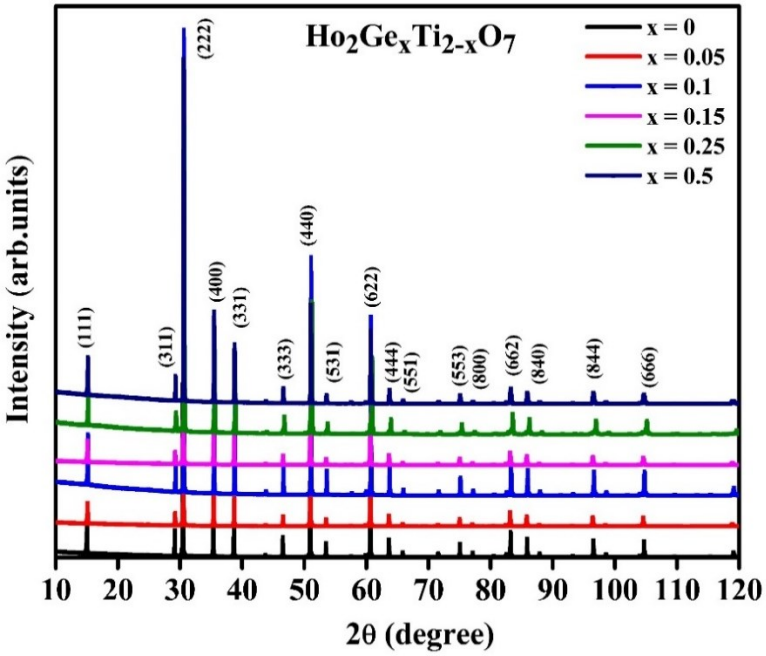

Figure 2.6 Room temperature high resolution x-ray diffraction pattern (HRXRD) pattern for $Ho_2Ge_xTi_{2-x}O_7$ (x = 0, 0.05, 0.1, 0.15, 0.25 & 0.5).

2.4 Characterization techniques

The following section deals with the various characterization tools adopted for studying the structural, magnetic, electronic and optical properties of the synthesized samples.

2.4.1 x-ray diffraction (XRD)

x-ray diffraction (XRD), a non-destructive technique primarily employed to determine the crystallographic properties of a particular material. In this technique, an electromagnetic wave having the wavelength 1-2 Å is scattered from the crystal lattice. XRD essentially facilitates the measurements regarding crystallographic phase identification, phase quantification, percent crystallinity, crystallite size and strain, lattice parameters and atomic structure.

XRD works on the principle of Bragg's law which states that the incident x-rays are diffracted from a set of equally spaced lattice planes in the crystal that interfere constructively. When the path difference between them is an integral multiple of the x-ray wavelength, these scattered x-rays interfere constructively. This can be mathematically expressed as follows:

$$2d_{hkl}\,\mathrm{Sin}\theta = \lambda \qquad (2.1)$$

where, d_{hkl} is the interplanar distance for a set of planes having Miller indices hkl, θ is the Bragg's angle, and λ is X-ray wavelength. An illustration of the Bragg's law is demonstrated in **Figure 2.7** [69]. Following the constructive interference between the scattered beams, the diffraction pattern exhibits high intensity peaks at certain scattering angles. In general, the diffraction peaks depend on the symmetry of structure, the crystals which possess low symmetry structure, say, monoclinic reveal several diffraction peaks because of numerous lattice planes while in the case of high symmetry structure (cubic and tetragonal) containing

certain lattice planes, a relatively lesser number of diffraction peaks are observed. The nature of diffraction peaks and their intensities are also correlated with the size and shape of particles in the crystal.

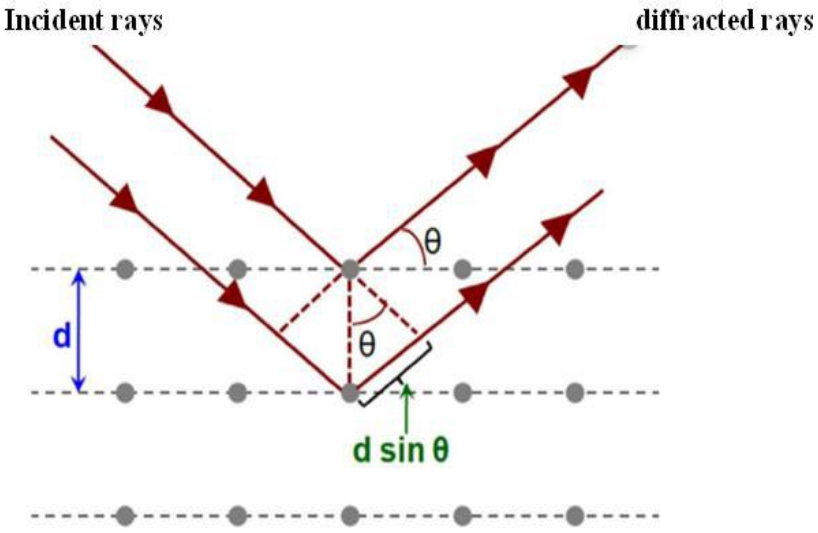

Figure 2.7 Schematic representation of incident and diffracted X-rays from the crystal lattice.

The instrumentation part of XRD contains four different sections:

1) x-ray production

2) x-ray diffraction from the crystal

3) Detection of diffracted x-rays and

4) XRD data recording and analysis.

In this instrument, the x-rays are produced when an accelerated electron beam of required energy is directed towards the metal target. The obtained collimated characteristic x-rays are

utilized to characterize the material. Most of the diffractometer works on the para-focusing (or Bragg-Brentano) configuration. This geometry is the most common and well suited for different materials. Diffracted beams are measured into a count rate which is essentially converted by the detector. The detector and sample can rotate by an angle 2θ and θ, respectively. Finally, the plot consisting of a series of diffraction peaks which are function of diffraction angle is realized that can be used for analysis of the crystal structure. Usually, the XRD patterns are recorded in the range of $2\theta = (10 – 120)°$.

In our work, phase purity was examined at room-temperature using high-resolution x-ray diffraction (HRXRD) pattern obtained using x-ray diffractometer (Smart Lab 9 kW, Rigaku, Japan; Cu $K_{\alpha 1}$ radiation of 1.54059 Å. Structural analysis (space group and lattice parameter) and indexing of HRXRD patterns was done using Rietveld refinement through FULLPROF SUITE [70]. Line shapes of various Bragg reflections were modeled using the Pseudo-Voigt profile shape function. This fitting technique is based on matching the suitable generated intensities based on the input parameters, with experimental data to determine the particular crystal structure of a specific space group. Eventually, different structural parameters like lattice constants, cell volume, bond lengths and bond angles are extracted for the synthesized samples using the calculations tools embedded in VESTA (3d visualisation software) [71]. The background was fitted, applying the method of linear interpolation between the data points. The crysallographic details had been obtained through the Rietveld refinement method as described below.

A brief presentation of Rietveld refinement method:

This programme is used for structure profile refinement of x-ray powder diffraction data. This program is also used for profile matching of the diffraction pattern without the knowledge of the structure. To extract all the possible correct information from the diffraction patten related to the sample, a computer program developed by Dr. H. Rietveld is utilized, known as 'Rietveld refinement', 'Rietveld analysis' or 'Reitveld method'.

The refinements are carried out until the best fit is obtained between the entire observed powder diffraction pattern taken as a whole and the entire calculated pattern based on the simultaneously refined model for the crystal structure, diffraction optics effect, instrumental factors and other specimen characteristics [72]. The parameter which is sought to be minimized is the residual, Sy:

$$S_y = \sum_i w_i \, (y_{oi} - y_{ci})^2 \qquad (2.2)$$

where, y_{oi} is the observed and y_{ci} is the calculated intensity at the i^{th} step and w_i is a suitable weight given by $(w_i)^{-1} = y_{oi}$.

A powder diffraction pattern results from several individual reflections, each of which has a peak height, a peak position, a breadth, tails which decay gradually with distance from the peak position, and an integrated area which is proportional to the Bragg Intensity I_k of each reflection where k stands for the Miller indices h, k, l. The intensity I_k is proportional to the square of the structure factor ($I_k \alpha |F_k|^2$) [72]. Typically, many Bragg reflections contribute to the intensity, y_i, observed at any arbitrarily chosen point 'i' in the powder diffraction pattern. The calculated intensities y_{ci} are determined from the $|F_k|^2$ values calculated from the

proposed structural model by summing up the calculated contributions from the neighboring Bragg reflections plus the background:

$$y_{ci} = s \sum L_k |F_k|^2 \Phi(2\theta_i - 2\theta_k) P_k A + y_{bi} \quad (2.3)$$

where s is the scale factor, k represents the Miller indices, h, k, l, for a Bragg reflection, L_k contains the Lorentz, polarization, and multiplicity factors, Φ is the reflection profile function, P_k is the preferred orientation function, A is an absorption factor, F_k is the structure factor for the k^{th} Bragg reflection, and y_{bi} is the background intensity at the i^{th} step [72]. The Rietveld technique is a structure refinement technique where the knowledge of the basic structure is required in advance. In recent years, however, attempts have been made to solve unknown structures also using this technique [73]. The shape of a powder diffraction reflection is influenced by both the sample (e.g., domain, size, stress/strain, defects) and the instrument (e.g., radiation source, geometry, slit sizes), and they vary as a function of 2θ. Among the various peak shape functions, the pseudo-Voigt, an approximation of the Voigt function, is most widely used. The pseudo-Voigt (pV) function is simply a linear combination of Lorentzian (L) and Gaussian (G) components in the ratio [72]

$$pV = \eta L + (1-\eta)\, G \quad (2.4)$$

where, η is the pseudo-Voigt mixing parameter. All peak shape functions contain half width of the Bragg peaks or the full width at half maxima (FWHM) whose angular dependence is expressed by the famous Coglioti function [74]:

$$(FWHM)^2 = U\tan^2\theta + V\tan\theta + W \quad (2.5)$$

where, U, V and W are half width parameters.

The parameters which are refined in the Rietveld method include structural parameters (positional coordinates, unit cell parameters and thermal parameters), sample parameters (strains, domain size, preferred orientation), instrumental parameters (FWHM of the peaks due to diffraction geometry, shift of origin, background etc.) and the scale factor. Rietveld refinement process will adjust the refinable parameters until a 'best fit' for the entire calculated pattern to the entire observed pattern is obtained. It is important to check the adequacy of the selected structural model in giving global minima, rather than local ('false') minima, in the agreement factors. One needs various criteria of fit usually called agreement factors, in order to make these choices. The indicators used in the refinements are the various R-factors (or agreement factors) which are defined as follows [72]:

(i) R- structure factor $:R_F=\frac{\sum|(I_K(obs'))^{\frac{1}{2}}-I_K(cal)^{\frac{1}{2}})|}{\sum(I_k(obs'))^{\frac{1}{2}}}$

(ii) R-profile factor $:R_p=\frac{\sum|y_{oi}-y_{ci}|}{\sum y_{oi}}$

(iii) R-Bragg factor $:R_B=\frac{\sum|I_K(obs')-I_K(cal)|}{\sum(I_k(obs'))}$

(iv) R-Weighted profile factor $:R_{wp}=\left\{\frac{\sum wi(y_i(obs)-y_i(cal))}{\sum w_i(y_i(obs))^2}\right\}^{1/2}$

(v) R-expected weighted profile factor $:R_{exp}=\left[\frac{(N-P)}{\sum w_i y2_{oi}}\right]^{1/2}$

In the above expressions I_K is the intensity assigned to the K_{th} Bragg reflection at the end of the refinement cycles. N and P are number of observations and variables. The Bragg intensity I_K is rarely observed directly. Therefore, the I_K values in the expression for R_F and R_B are obtained from the total observed intensity using programmatic allocation which is generally biased towards the structural model being refined.

The goodness -of- fit indicator 'S' can be given as

$$S=\frac{R_{WP}}{R_e}=\left[\frac{S_y}{(N-P)}\right]^{1/2} \quad (2.6)$$

The S value depends on the quality of powder diffraction data and is only an indicator of the global minimum solution. Irrespective of the S value, one seeks to achieve a difference profile as flat as possible before accepting a model. The goodness of fit of the system is also represented by an indicator called χ^2 and expressed as

$$\chi^2=S^2=\left[\frac{R_{wp}}{R_{exp}}\right]^2=\left[\frac{S_y}{(N-P)}\right] \quad (2.7)$$

From purely mathematical point of view, R_{WP} is the most meaningful among all the agreement factors.

2.4.2 Synchrotron x-ray diffraction (SXRD)

Synchrotron x-ray diffraction (SXRD) measurement has been carried out for low temperature structural analysis using Reitveld refinement of the obtained diffraction pattern. The data was collected at P24 beamline at PETRA-III (DESY), Hamburg, Germany. The diffraction pattern was obtained using 25 keV x-ray radiation source in a temperature range of (15-150) K .

2.4.3 Magnetic Measurements

Magnetic properties of the synthesized magnetically frustrated systems were investigated by means of field dependent magnetization (M-H), temperature dependent magnetization (M-T) and ac-susceptibility measurements using Magnetic Properties Measurements System. This instrument uses vibrating sample magnetometer (VSM) and the Superconducting Quantum Interference Device (SQUID) to measure the magnetic moments of the systems. The

magnetic measurements were performed at (SQUID) magnetometer (MPMS-3) of Quantum Design, Inc U.S.A at Centre Instrument Facility (CIF), IIT (BHU), India. The magnetic moment of the samples is measured along with sustaining excellent accuracy for highly sensitive samples using SQUID. [75].

SQUID Magnetometer

For measuring the magnetic moment in the specimen, SQUID is the most suitable and sensitive technique. This device measures very small magnetic field with the help of superconducting loops which are Josephson junction. Specifically, SQUID indirectly measures the magnetic field of specimen. In general, when the specimen passes through superconducting detection coils connected with the SQUID via superconducting wires, it enables the flow of current from the detection coils to inductively coupled high quality sensors. The current from these coils is converted to equivalent voltage through SQUID. The whole assembly of instrumentation can be divided into following primary components: SQUID (main device), a magnetic flux transformer with appropriate detection coils, the superconducting magnetic coil and heat switches including suitable magnetic shielding configuration. Superconducting detection coils do not response to uniform and linear magnetic fields since the coils are set as second-order gradiometer having counter wound outer loops. When the local magnetic field changes, it produces a certain current in the detection coils. In practical situation, SQUID can response to every small change in the magnetic field. For this reason, the magnetic shielding is of utmost importance to prevent the sensor detecting stray fields arising from ambient or laboratory or the large magnetic fields originating from superconducting coil. The small area where magnetic field changes in detection coils, heaters are used to remove the standing currents in the superconducting loops

by raising them beyond their critical temperature. SQUID offers remarkable sensitivity of 5 x 10^{-8} emu and frequency range of 0.1 - 1 kHz. The measurement and removal of background ac phase shifts for each measurement is done through direct phase nulling technique. The rate of temperature change is 10 K/min while cooling 300 to 10 K and further cooling till 2 K is performed at 2 K/min.

M-T data of the synthesized powder samples were collected at an applied magnetic field of 100 and 1000 Oe in the temperature range of (2-300) K using standard protocols for zero-field-cooled (ZFC) and field-cooled (FC) measurements. The magnetization vs. field (M-H) measurements was performed at a temperature of 2 K for magnetic field ranging from -70 to 70 kOe. The ac-susceptibility data were collected in the temperature range of (2-100) K at varying frequency between (50-900) Hz. The applied dc bias was varied from 0-50 kOe.

ac- susceptibility

ac susceptometry utilizes the effect of a changing magnetic flux inducing a voltage in a detector/sensing coil (Faraday's law) and use the magnetization of a sample to generate this changing flux. a.c. measurements generate a changing flux due to the applied a.c. magnetic field yielding a time-varying response in the sample with the sample kept stationary.

In a.c. magnetic susceptibility, a time-varying sinusoidal magnetic field of amplitude $H_{a.c.}$ (typically 0.5 mT) is applied to the sample. Simultaneously, a static d.c. magnetic field ($H_{d.c.}$) may also be applied, though often this is set to zero (and the a.c. measurement is directly probing the ground state of the spin system due to small a.c. amplitude). Thus the field H inside the sample is given as [76]

$$H = H_{d.c.} + H_{a.c.} \cos(\omega t) \quad (2.8)$$

where ω (=2πν) is the frequency of the oscillating magnetic field. The frequency ν is typically in the range of 0.1-10^4 Hz and so probes the processes which are faster than those studied by the magnetic relaxation technique described above. The oscillating response of the magnetization is recorded ($M_{a.c.}$), and the ac-susceptibility is then defined as

$$\chi_{a.c.} = M_{a.c.} / H_{a.c.} \tag{2.9}$$

When the frequency of the oscillating magnetic field is comparable to the timescale of the magnetic relaxation of the system, it offers a complex response. In this regime, there may be some lag (therefore dissipation) when the perturbation is slightly faster or slower than the natural frequency of the system. Thus, the response is described as consisting of two parts: in-phase (real) and out-phase (imaginary) components, i.e., $\chi'_{a.c.}$ and $\chi''_{a.c.}$ The imaginary component is related to the dissipation in the system. The ac-susceptibility is represented as a complex number

$$\chi_{a.c.} = \chi'_{a.c.} + i\,\chi''_{a.c.} \tag{2.10}$$

ac-susceptibility measurements of the spin-ice show an Arrhenius-like behavior at high temperature (due to single ion processes and mixing with excited states), but on cooling, the dynamics begin to freeze out.

2.4.4 Density Functional Theory (DFT)

DFT is a very effective technique for studying molecules, nanostructures, solids, surfaces and interfaces, by directly solving approximate versions of the Schrödinger equation.

The time-independent Schrödinger equation takes the following symbolic form [77]:

$$(\text{Kinetic energy} + \text{potential energy})\,\Psi = E_{tot}\Psi \tag{2.11}$$

$$[p^2/2m_e+V(r)]\,\Psi(r) = E\,\Psi(r) \tag{2.12}$$

$$\text{Kinetic energy} = -\sum_{i=1}^{N}\frac{\hbar^2}{2m_e}\nabla_i^2-\sum_{I=1}^{M}\frac{\hbar^2}{2M_I}\nabla_I^2. \tag{2.13}$$

In case of derivatives in the Laplace operators ∇^2 is taken with respect to the coordinates of each particle.

$$\nabla^2\Psi = \frac{\delta^2\Psi}{\delta x_1^2}+\frac{\delta^2\Psi}{\delta y_1^2}+\frac{\delta^2\Psi}{\delta z_1^2} \tag{2.14}$$

For the potential energy term; firstly, we have the Coulomb repulsion between electron pairs given as:

$$(\text{Potential energy})_{ec} = \tfrac{1}{2}\sum_{i\neq j}\frac{e^2}{4\pi\epsilon_\circ}\frac{1}{|r_i-r_j|} \tag{2.15}$$

Here the indices *i* and *j* run from 1 to *N*. The terms $i = j$ is excluded because an electron does not repel itself, and we divide by 2 in order to count only one contribution per pair.

Secondly, we have the Coulomb repulsion between pair of nuclei:

$$(\text{Potential energy})_{nn} = \tfrac{1}{2}\sum_{i\neq j}\frac{e^2}{4\pi\epsilon_\circ}\frac{Z_I Z_J}{|R_I-R_J|} \tag{2.16}$$

Here the indices *I* and *J* run from 1 to *M* and the Z_I represent the atomic numbers.

Third, we have the Coulomb attraction between electrons and nuclei:

$$(\text{Potential energy})_{nn} = -\sum_{i,I}\frac{e^2}{4\pi\epsilon_\circ}\frac{Z_I}{|r_i-R_I|} \tag{2.17}$$

with *i* from 1 to *N* and *I* from 1 to *M*. At this point we can combine equations from 1 to 6 and write the many-body Schrödinger equation:

$$[-\sum_{i=1}^{N}\frac{\hbar^2}{2m_e}\nabla_i^2-\sum_{I=1}^{M}\frac{\hbar^2}{2M_I}\nabla_I^2+\tfrac{1}{2}\sum_{i\neq j}\frac{e^2}{4\pi\epsilon_\circ}\frac{1}{|r_i-r_j|}+\tfrac{1}{2}\sum_{i\neq j}\frac{e^2}{4\pi\epsilon_\circ}\frac{Z_IZ_J}{|R_I-R_J|}+-\sum_{i,I}\frac{e^2}{4\pi\epsilon_\circ}\frac{Z_I}{|r_i-R_I|}]\Psi = E_{\text{tot}}\Psi \quad (2.18)$$

From US National Institute of Standards and Technology database the values are as such:

$\hbar = 1.05457163 \times 10^{-34}$ Js

$m_e = 9.10938291 \times 10^{-31}$ kg,

$m_p = 1.67262164 \times 10^{-27}$ kg,

$e = 1.60217649 \times 10^{-19}$ C,

$\epsilon_0 = 8.85418782 \times 10^{-12}$ F/m

Now using,

1 Ha = 27.2114 eV = 4.3597×10^{-18} J,

1 bohr = 0.529177 Å = 0.529177×10^{-10} m,

1 a.u. of mass = $9.10938291 \times 10^{-31}$ kg,

where 'Ha' stands for Hartree and 'a.u.' for atomic unit. Taken together these units form the so-called Hartree atomic units. In Hartree atomic units the many-body Schrödinger equation acquires the following elegant form:

$$[-\sum_i\frac{\nabla_i^2}{2}-\sum_I\frac{\nabla_I^2}{2M_I}+\tfrac{1}{2}\sum_{i\neq j}\frac{1}{|r_i-r_j|}+\tfrac{1}{2}\sum_{i\neq j}\frac{Z_IZ_J}{|R_I-R_J|}+-\sum_{i,I}\frac{Z_I}{|r_i-R_I|}]\Psi = E_{\text{tot}}\Psi \quad (2.19)$$

This is the most commonly used form of the many-body Schrödinger equation in first-principles materials modeling. This equation shows very clearly that the only external parameters needed in this approach are the atomic numbers, Z_I, and the atomic masses, M_I.

Now applying various approximations on this namely clamped nucleus approximation, independent electron approximation, exclusion principle, mean field approximation, Hartree-Fock equations we arrive at Kohn-Sham equation:

$$[-\frac{\nabla^2}{2} + V_n(r) + V_H(r) + V_x(r) + V_c(r)]\ \varphi i(r) = \varepsilon_i \varphi_i(r) \quad (2.20)$$

Where V_n is the external nuclear potential, V_H is the Hartree potential and kinetic energy term is given by $-1/2\nabla^2$,

$$V_n(\mathrm{r}) = -\sum_I \frac{Z_I}{|r - R_I|} \quad (2.21)$$

And Hartree potential is given as:

$$n(\mathrm{r}) = \sum_i |\Phi_i(r)|^2 \quad (2.22)$$

$$\nabla^2 V_H(r) = -4\pi n(r) \quad (2.23)$$

The above-described Kohn–Sham equations are central to first principles materials modeling. V_x and V_c is called the exchange and correlation potential given as:

$$V_{xc}(\boldsymbol{r}) = \delta E_{xc}[n]/\delta n\ |n(r)| \quad (2.24)$$

The external nuclear potential, kinetic energy and the Hartree energy constitutes the total energy in the independent electron approximation. The practical usefulness of ground-state DFT depends entirely on whether approximations for the functional $E_{xc}[n]$ could be found which are at the same time sufficiently simple and accurate.

In order to introduce such a functional, it is convenient to study the exchange and correlation energy of a very simple system, the homogeneous electron gas. This system is closely related to the 'free electron gas' whereby a gas of electrons is constrained within a box and the potential of the nuclei is taken as constant. This approximation is known as local density approximation (LDA). The plane wave cut-off energy is given through LDA-1/2 approximation where 1/2 of the electronic charge is subtracted from the ion's topmost orbitals

[78]. The functional form of the exchange and correlation energy is further improved taking into account not only the density, but also its gradients and this approximation is called generalized gradient approximation (GGA).

To model the electronic structure of $Ho_2Ti_2O_7$, $Ho_2Ge_2O_7$, and $Ho_2Ge_xTi_{2-x}O_7$, Density Functional Theory (DFT) calculations were performed using the Quantum-ESPRESSO [79], which uses a plane-wave basis set, and pseudopotential. We use Rappe-Rabe-Kaxiras-Joannopoulos (RRKJ) flavor of ultra-soft pseudopotentials to treat the interaction between the ion cores and the valence electrons. For the exchange-correlation interactions we employ the local density approximation (LDA). The ground state electronic configurations for the pseudopotential generation of the constituent atoms are noted as follows: Ho =[Xe] $4f^{10}$ $5d^{1.0}$ $6s^{1.5}$ $6p^{0.5}$, Ge = [Ar] $3d^{10}$ $4s^2$ $4p^2$, Ti=[Ar] $4s^2$ $4p^0$ $3d^2$, and O = [He] $2s^2$, $2p^4$. We did not include the effects of spin orbit coupling in atoms. Scalar-relativistic pseudopotentials that account for most of the relativistic effects have been used for the present calculations. Also, for this calculation the focus is on the optical properties, spin polarized DFT calculations has been excluded. We have used tetragonal unit cell of the base $Ho_2Ge_2O_7$ with the space-group $P4_12_12$. The following experimental lattice parameters were taken as the input: a = b = 6.850 Å, c = 12.477Å, and α = β = γ = 90°.We have use variable-cell optimization to relax the cell parameters and atomic positions, until the forces on each atom are less than 0.5 mRy/bohr, and the pressure is less than 0.05 GPa. Kinetic energy cut-offs of 50 Ry for the wave functions and 500 Ry for the charge densities are found to be sufficient for an accurate determination of the structure. For a cubic unit cell of $Ho_2Ti_2O_7$ and $Ho_2Ge_2O_7$, 6× 6× 6 k-point grid was found to be sufficient for accurate calculation of structural and electronic properties, whereas for a tetragonal unit cell, 4 × 4 × 2 k-point grid was good enough. The computed lattice

parameters from LDA-DFT are underestimated by a few percent, which is along the expected line. The fully relaxed $Ho_2Ge_2O_7$ lattice parameters are as follows: a = b = 6.678 Å, c = 12.168 Å, and α = β = γ = 90°.Within the base tetragonal structure of $Ho_2Ge_2O_7$, we varied the Ti: Ge ratio through substitutional replacement of Ge by Ti atom, thereby we varied the stoichiometry. Subsequently, the structure has been fully relaxed. Post variable cell relaxation, the deviation from tetragonal structure has been noted. The band structure changes, as there is symmetry breaking due to alloying with Ti. It has been observed that with increase in the Ti in $Ho_2Ge_2O_7$, the band gap monotonically decreases. The band extrema also change from the parent $Ho_2Ge_2O_7$. The simulated lattice parameters for $Ho_2Ti_{0.5}Ge_{1.5}O_7$ are as follows a = 6.716 Å, b= 6.722 Å, c = 12.148Å, α =90.49, β = 89.24, γ = 90.06. The simulated lattice parameters for $Ho_2Ti_{1.0}Ge_{1.0}O_7$ are as follows a = 6.789Å, b= 6.736Å, c = 12.102Å, α = 89.43, β = 89.45, γ =89.99. The simulated lattice parameters for $Ho_2Ti_{1.5}Ge_{0.5}O_7$ are as follows a = b= 6.830Å, c = 11.945Å, α = 89.43, β =90.84, γ =90.07.

Since the standard DFT is known to notoriously underestimate the band gap by as much as 50% or more, in our modeling approach to the band structure, we went beyond standard DFT and used a method called LDA-1/2 technique which is based on Slater's transition state theory[80][81]. This technique is used for correcting the self-energy contribution to the electronic excitation energy in the LDA-DFT. The self-interaction correction is carried out at the atomic pseudo potential level, thereby leading to the solid-state calculations with corrected band gap. However, this method requires us to find a CUT radius (energy cut-off radius; energy that determines the size of the plane wave basis set) for each atomic pseudo potential for which the band gap of the system is optimal. The advantage of this method over the other known methods such as the GW, (which includes the Green's Function G and screened

Coulomb Interaction W) and the hybrid functional approaches is that the calculation of corrected band gap comes out with the computational cost of standard LDA-DFT [82][78]. We have used the LDA-1/2 pseudopotentials for Ge, Ti, and O atoms, whereas the Ho atom pseudopotential is of standard LDA functional.

2.4.5 x-ray electron spectroscopy (XPS)

XPS, also known as electron spectroscopy for chemical analysis (ESCA), is used for elemental investigation, oxidation state of the constituent elements and valence band structure by probing the surface of specimen. It is a surface sensitive technique so it provides essentially the relative composition of the constituents in surface regime. XPS works on the principle of photoelectric effect in which the emission of electron occurs when the core level electrons are excited by energetic X-ray photons of energy, hν. The kinetic energy (K.E.) of electrons emitted in such situation is expressed as follows:

$$K.E. = h\nu - B.E. - \phi \tag{2.25}$$

where B.E. is the binding energy of an individual electron and ϕ is the work function. Explicitly, the photoelectrons are emitted from the core levels when the energy of X-ray photon is larger than the binding energy of the electron. The identification of these photoelectrons is based on their respective kinetic energy. The XPS spectra are drawn between the frequency of emitted electrons as a function of their K.E and intensity. The B.E. of different electronic states is calculated with respect to the Fermi energy level. For certain photon energy, the K.E. distribution of the photoelectrons implies the energy distribution of electronic states. These photoelectrons are usually scattered from nearby electrons, plasmons and/or phonons that slows down energetic electron since they are adhered to partial loss of

energy. Due to significant loss in energy, the photo excited electrons do not pass through the specimen. This undesirable scattering of photoelectron results into unwanted secondary inelastic background intensity. Such scattering is more prominent within the low range of kinetic energy occurring because of strong electron-electron interaction. Although X-ray can penetrate up to large depth into specimen, only the photoelectrons originating from a depth of a few tens of angstrom can be detected due to high degree of scattering. After the collision or scattering, photoelectrons with sufficient kinetic energy surpass the work function barrier and reach the detector. XPS consist of three different parts namely:

(i) a photon source,

(ii) an energy analyser for photoelectrons, and

(iii) an electron detector.

In general, the scattering and collisions between emitted electrons is reduced when the chamber is evacuated to ultra-high vacuum. This enhances the mean free path of the emitting electrons which easily reaches to the detector. The monoenergetic soft X-rays are more appropriate energy source for exciting the photoelectrons. A compatible electrostatic analyzer is used to analyse the excited photoelectrons.

Core levels were studied using X-ray photoemission spectroscopy (XPS) with Al K_α source from SPECS (XR 50) at Indus-2, RRCAT. The scanning is first carried out to collect the complete range of energy i.e., survey scan. Afterwards, for the precise elemental analysis O, Ho, Ge & Ti core level spectra are selectively recorded. All the recorded core level spectra are calibrated with respect to C 1s peak centered at ~284.8 eV.

2.4.6 Ultraviolet Photoelectron Spectroscopy (UPS)

The valence band spectra were obtained through Ultraviolet Photoelectron Spectroscopy (UPS) using photon energy of 21.2 eV "He-I" at the experimental station of angle resolved photoelectron spectroscopy (ARPES), Indus-2, RRCAT. The sample was initially loaded in the lock chamber and a vacuum of 10^{-8} mbar was attained before it was transferred to the preparation chamber having the base vacuum of 5 X 10^{-11} mbar. The atmospheric oxygen and carbon from the sample surface was removed by very mild sputtering at 1 keV with Argon ions for 10 minutes. The UPS data has been recorded using SPECS (UVS 300) source and SPECS Phibos 150 electron energy analyzer. The base vacuum during the measurement was 9 X 10^{-11} mbar. The position of the Fermi edge in these samples was calibrated with the Fermi edge of standard silver foil. The background in UPS has been subtracted from the raw data using the Tougard procedure.

2.4.7 UV Visible absorption Spectroscopy

A UV Visible spectrophotometer comprises a light source, a monochromator, a sample holder and a photodetector that is used to obtain the absorption spectrum followed by the sample illumination using light in the ultraviolet-region. There are two possible optical arrangements namely single beam and double beam. White light (polychromatic) from a light source is introduced into monochromator and dispersed through diffraction grating. Light of only specific wavelength is emitted from exit slit. For a single slit I/I° is the transmittance where I° is the irradiated monochromatic light and I is the intensity of the detected transmitted light. For double beam, I and I° can be simultaneously obtained where the monochromatic light is divided into two using beam splitter and are allowed to pass through a reference and sample.

The measured value is the ratio of intensities of the two beams. Optical diffused reflectance spectra for $Ho_2Ge_xTi_{2-x}O_7$ polycrystalline samples in the range 220 - 1400 nm were collected at room temperature with a double beam UV-Visible spectrophotometer (SHIMADZU-2450). A white standard of barium sulphate was used as a reference. The intensity of beam that passes through reference is considered to be 100% transmission or zero absorbance. Absorption spectra were calculated from the reflectance data using Kubelka – Munk function. The energy band gap of the samples has been calculated using the value of absorption coefficient in the Tauc equation.

2.4.8 Photoluminescence emission Spectroscopy

Photoluminescence (PL) is emission of certain wavelength of light when the sample is exposed to light through three main processes namely excitation, relaxation and emission. This is the non-destructive technique used to study the electronic states of various materials. If a light particle (photon) has energy greater than the band-gap energy, then this energy is absorbed by the electron of valence band (V.B.) through photo-excitation process. This optical excitation leads to the transfer of electron to allowed excited states of conduction band (C.B.) across the forbidden energy gap as shown in **Figure 2.8**. The electron loses its excess energy through non-radiative relaxation (does not produce light) while coming to lowest energy state in the C.B. After this point, the electron eventually falls back to the V.B. and the energy lost is converted back into a luminescent photon which is emitted from the material. The intensity of this emitted photon is obtained as a function of wavelength. Hence, the direct measure of the band gap energy, (E_g) is extracted from the energy of the emitted photon. This entire photon excitation followed by photon emission is termed as photoluminescence.

Luminescence spectra has been recorded using Hitachi F-4600 Fluorescence spectrometer with Xenon lamp as an excitation source.

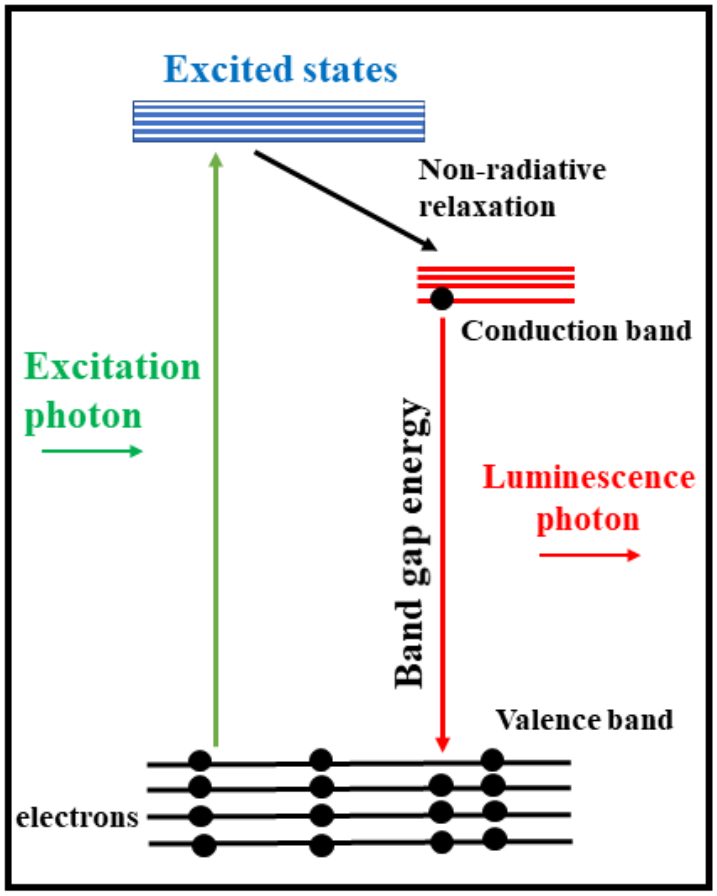

Figure 2.8 Schematic representation of photoluminescence emission.

For PL spectroscopy measurements, generally laser light or xenon lamp is used as the excitation source having variable energy. At a certain wavelength known as excitation wavelength, the specimen can produce the emission spectrum characteristic of the materials. PL spectrofluorometer measures and collects the spectra of fluorescence and phosphorescence from the sample. During the fluorescence mode, the excitation and emission spectra are

recorded for a range of wavelength. A standard fluorescence spectrometer contains following main components:

Illumination source: - The source of light in PL, is a continuous source of light which is obtained either by broadband xenon lamp or by monochromatic laser. The light originating from light source is collimated with the help of a set of elliptical mirrors along with lenses and then it is delivered to the entrance slit of the excitation monochromators via optical fibres. A window made of quartz separates the light source and excitation monochromators. This window is also used to release out the excess heating that may damage the light source.

Monochromators: - There are two monochromators exist in PL one is excitation monochromator and other one is emission monochromator. These monochromators offer high resolution for the complete wavelength range.

Gratings: - In the monochromator, for the di-reflection grating is used to disperse the incident light occurring because of the embedded vertical grooves and provides a good spectral resolution. MgF_2 layer onto these gratings prevents the unwanted oxidation.

Slits: - Entrance and exit slits are in both the monochromators for controlling the required amount of light. At the excitation monochromator, slit width allows certain band of light to transfer towards the sample. The slit at emission monochromator can be adjusted for signal intensity at the detector. The maximum intensity maintaining a high resolution over the whole spectral range is produced when an appropriate slit width is used.

Detectors: - There are two types of detectors are used in the spectrofluorometer one is reference detector and other is signal detector. A reference detector is used for the light source and signal detector is used transferring the signal to the photon counting module.

So, this chapter summarizes the working principle of the experimental tools along with the measurement protocols followed to characterize the systems. Now the results on structural and magnetic properties of $Ho_2Ti_2O_7$ is presented in the next chapter.